Acta Biomaterialia 170 (2023) 580–595

Contents lists available at ScienceDirect

Acta Biomaterialia

journal homepage: www.elsevier.com/locate/actbio

Full length article

Hydroxyapatite 3D-printed scaffolds with Gyroid-Triply periodic minimal surface (TPMS) porous structure: Fabrication and an *in vivo* pilot study in sheep

Islam Bouakaz[a,b], Christophe Drouet[b,*], David Grossin[b], Elisabeth Cobraiville[a], Grégory Nolens[a,c,**]

[a] CERHUM - PIMW, 4000 Liège, Belgium
[b] CIRIMAT, Université de Toulouse, CNRS / Toulouse INP / UT3, 31030 Toulouse, France
[c] Faculty of Medicine, University of Namur, 5000 Namur, Belgium

ARTICLE INFO

Article history:
Received 14 April 2023
Revised 17 August 2023
Accepted 21 August 2023
Available online 9 September 2023

Keywords:
Bone scaffolds
TPMS
Gyroid
Hydroxyapatite
Large animal model
Additive manufacturing

ABSTRACT

Bone repair is a major challenge in regenerative medicine, e.g. for large defects. There is a need for bioactive, highly percolating bone substitutes favoring bone ingrowth and tissue healing. Here, a modern 3D printing approach (VAT photopolymerization) was exploited to fabricate hydroxyapatite (HA) scaffolds with a Gyroid-"Triply periodic minimal surface" (TPMS) porous structure (65% porosity, 90.5% HA densification) inspired from trabecular bone. Percolation and absorption capacities were analyzed in gaseous and liquid conditions. Mechanical properties relevant to guided bone regeneration in non-load bearing sites, as for maxillofacial contour reconstruction, were evidenced from 3-point bending tests and macrospherical indentation. Scaffolds were implanted in a clinically-relevant large animal model (sheep femur), over 6 months, enabling thorough analyses at short (4 weeks) and long (26 weeks) time points. *In vivo* performances were systematically compared to the bovine bone-derived Bio-Oss® standard. The local tissue response was examined thoroughly by semi-quantitative histopathology. Results demonstrated the absence of toxicity. Bone healing was assessed by bone dynamics analysis through epifluorescence using various fluorochromes and quantitative histomorphometry. Performant bone regeneration was evidenced with similar overall performances to the control, although the Gyroid biomaterial slightly outperformed Bio-Oss® at early healing time in terms of osteointegration and appositional mineralization. This work is considered a pilot study on the *in vivo* evaluation of TPMS-based 3D porous scaffolds in a large animal model, for an extended period of time, and in comparison to a clinical standard. Our results confirm the relevance of such scaffolds for bone regeneration in view of clinical practice.

Statement of significance

Bone repair, e.g. for large bone defects or patients with defective vascularization is still a major challenge.

Highly percolating TPMS porous structures have recently emerged, but no *in vivo* data were reported on a large animal model of clinical relevance and comparing to an international standard.

Here, we fabricated TPMS scaffolds of HA, determined their chemical, percolation and mechanical features, and ran an in-depth pilot study in the sheep with a systematic comparison to the Bio-Oss® reference.

* Corresponding author at: CIRIMAT laboratory, University of Toulouse, France, Mailing address: CIRIMAT-ENSIACET, 4 allée Emile Monso, 31030 Toulouse Cedex 4, France.
** Corresponding author at: CERHUM/University of Namur, Belgium, Mailing address: CERHUM – PIMW, B56, 1 Rue des pôles, 4000 Liège, Belgium.
E-mail addresses: christophe.drouet@cirimat.fr (C. Drouet), gregory.nolens@cerhum.com (G. Nolens).

https://doi.org/10.1016/j.actbio.2023.08.041

Our results clearly show the high bone-forming capability of such scaffolds, with outcomes even better than Bio-Oss® at short implantation time. This preclinical work provides quantitative data validating the relevance of such TMPS porous scaffolds for bone regeneration in view of clinical evaluation.

1. Introduction

In humans, as in all vertebrates, bones ensure the overall mechanical stability of the organism and allow its mobility while protecting vital organs. The mineral part of bone also actively contributes to homeostasis processes upon interaction with body fluids in order to maintain healthy concentration equilibria of dissolved ionic species [1–3]. These features are imparted by the two main components of the bony matrix, namely a (nonstoichiometric) hydroxyapatite phase composing the bone mineral and representing about 70 wt.% of bone matter, and collagen standing for about 20 wt.% [4–6]. In bone physiology, the interconnected 3D porous network of the trabecular bone matrix is in particular essential to favor cell activity, not only for bone remodeling but also for other functions such as the production of bone marrow encompassing blood cells [7].

Skeletal traumas and bone diseases – e.g. in the case of osteoporosis (leading to poor calcification levels) or of bone cancers – may however dramatically alter the normal functions of bones, and this is increasingly problematic nowadays in link with the general aging of populations worldwide. Such conditions then necessitate surgical treatments for guided bone regeneration, with the view to ultimately reconstruct the bony architecture and its related functions. In this regard, autologous bone grafts are often considered as the “gold standard” because the grafted tissue originates from the patients themselves and thus perfectly corresponds to the target bone filling material [8,9]. However, such autografts are associated to higher morbidity [10,11] and overall pain, since a second “donor” surgical site (e.g. fibula or iliac crest) is necessary, which could further facilitate the spreading of pathogenic microorganisms to favor bone infections. Also, the amount of bone graft tissue remains limited and can thus only be addressed to repair small defects. Yet, large bone defects cannot heal spontaneously even with adequate care and surgical stabilization [12]. In this view, other strategies are thus needed to replace bone grafts by other materials accessible in larger amounts. Bone xenografts, i.e. originating from other animal species, are then a solution of choice to provide both a chemical composition and 3D open porous network that fit very well those of human bones. Bio-oss®, for example, is a bovine bone-derived biomaterial considered nowadays as a reference for bone repair, which was particularly well documented in maxillofacial surgery [13–19].

Despite such xenograft/animal-derived solutions, the need to develop synthetic bone substitutes remains high as they may prevent the use of animal tissues, for both ethical and sometimes religious reasons, as well as eliminate any issues of viral/prion transmission and also allow obtaining highly reproducible unlimited batches. To-date, there still remains the challenge of providing synthetic biomaterials exhibiting not only an intrinsic biocompatibility and possibly the capacity to provide a bone-inspired chemical composition, but also to offer a highly percolating porous network (as with natural bone trabeculae), as all of these features appear essential for optimal functions in bone sites.

Concerning biocompatibility, calcium phosphates (CaP) are particularly appealing, taking into account their similarity to the chemical composition of natural bone, and hydroxyapatite (HA) has in particular been widely used based on its crystal structure and composition close to biological apatite [20–23]. Regarding the percolating open porous network, it is increasingly seen as a key parameter for repairing complex or large bone defects. Indeed, among postoperative complications is the obstruction of the vascular supply in the surrounding soft tissue (skin and mucous membranes), which in turn reduces the bone repair ability and resistance to infections. Also, a high degree of porosity ($>$ 50%) is important to promote osteoconduction [24,25] by enhancing the migration, adhesion and proliferation of cells inside the biomaterial and facilitating the infiltration of body fluids that contain the growth factors and nutrients necessary for optimal bone cell activity [22,26]. Nonetheless, in addition to the overall degree of porosity, other parameters are also necessary for efficient osteoconduction, such as the size and shape of the pores and the degree of interconnection [27]. While smaller pores ($<$ 10 µm) offer a larger specific surface to favor cell and protein adhesion [28,29] and enhance ionic exchange [30,31], larger pore sizes are necessary to allow efficient vascularization [32] and the circulation of multinuclear cells like osteoclasts. Optimal macropore size and interconnectivity are still debated, but most authors advise macropore sizes above 300 µm [33] with interconnection sections wider than 100 µm [34]. Studies seeking to determine the upper limit of pore size and interconnection have only appeared in the last two decades. M.-C. von Doernberg et al. [35] studied a wide range of pore sizes 150, 260, 510 and 1220 µm. Their results showed a marginal difference in biological responses between these different pore sizes, with a stronger resorption for the 510 µm pore size. A more recent study by Li et al. [36] compared pore sizes of 500-600 µm, 750–900 µm and 1050–1200 µm, and showed that parts containing a pore size between 750 and 900 µm had a greater amount of newly formed bone tissue and neovascularization. These studies reduce the recommended range of macropore sizes to 750–900 µm; therefore, the pore size to be studied in this work will be 900 µm.

The study conducted by Mirkhalaf et al. [37] also highlighted the importance of interconnections by investigating various forms of porosity in rabbits. The results demonstrated that, at 12 weeks, bone formation is more affected by interconnections than by pore concavity. However, the study by Van Hede et al. [38] revealed the importance of pore shape especially in the first weeks after implantation in rats calvaria (4 and 8 weeks). Several other studies also pointed out pore shape as a non-negligible factor to influence the formation of blood vessels and cell migration: spherical pores were reported to favor tissue ingrowth in a superior way to polygonal pores [39], and globally concave surfaces were found more propitious to bone regrowth than convex and flat surfaces [30,40–42]. Taking into account the negative impact of porosity on mechanical properties, a conciliation has to be found for seeking optimal biological outcomes while exhibiting similar mechanical properties to trabecular bone [33]. 3D printing is one approach that could remediate this difficulty.

Ceramic 3D printing is a potential solution to address this challenge. This ceramic fabrication method emerged in the 1990s [43], and has evolved over the past three decades, giving rise to increasingly precise and controlled additive manufacturing technologies [44]. This development has gained momentum in recent years, leading to the emergence of companies in this field. Studies using

3D printing to explore new porosity have gradually proliferated, starting with relatively simple structures (such as tetragonal and cylindrical pores) [45], and progressing towards complex scaffolds that have emerged in recent years.

In this regard, Triply Periodic Minimal Surfaces (TPMS) are complex periodic structures found in nature (e.g. in some mitochondria [46] or butterfly wings [47] for example) that can meet all the above porosity criteria thanks to interfacial tensions that minimize the surface area between grain boundaries [48]. Mathematically described for the first time in 1865, these structures – which include for example the Gyroid system – offer a continuous tortuosity of highly interconnected pores giving rise to a high degree of concavity, improved permeability and reduced stress concentration. Plus, through the TPMS-generating mathematical equations, it is possible to tailor the overall porosity, pore size and wall thickness. Adaptation to bone substitutes allowed improving the osteoconduction through an optimized porosity [36] with a simultaneous control of the mechanical properties upon modulation of the wall thickness [49].

Progress in 3D printing technologies in the field of ceramics has permitted, over the last years, the fabrication of TPMS/Gyroid complex structures [38,50]. In particular, VAT polymerization has established among the most precise 3D printing technologies with a 25–50 µm resolution [51] while enabling the fabrication of denser/tougher pieces from precursor pastes with a high ceramic content [51]. However, in spite of these recent developments, the use of this technology to fabricate 3D-printed CaPs has not yet received the attention it deserves. In the case of HA, the accessible literature essentially deals with relationships between mechanical performances and geometrical parameters (pore size, wall thickness) [52,53]; and only a very limited number of reports dealt, to this day, with their biological evaluation. *In vitro*, TPMS structures – whether on CaPs or other compounds – were shown to enhance cell viability, seeding/attachment and proliferation [52,54,55]. In contrast, scarce *in vivo* studies have been reported on TPMS-structured biomaterials, and they almost all involved small animal models and generally limited timeframes: rats (calvaria over 7 weeks, femur over 8 weeks) and rabbits (femur over 12 weeks) for CaPs [38,53,56,57] and mini-pigs (tibia over 5 weeks for TA6V [58], meniscus over 12 weeks for polycarbonate polyurethane [59], mandible over 6 months for β-TCP [60]). There is an almost complete lack of data on large animals closer to human physiology to allow clinical translation, and over longer implantation periods to assess short- and long-terms bone repair performances. In any case, these pre-existing results on small animal models already points out the advantageous impact of TPMS advanced porous structures apt to provide faster osteointegration than conventional designs. One recent study from 2022 was reported in the sheep [61], but no comparison to conventional bone substitutes/references was given. The authors nonetheless confirmed the promise of 3D-printed Gyroid structures – of biphasic CaPs soaked in bone marrow in that study – illustrated for segmental mandibular bone defects.

In this context, the present study aimed at *i)* producing 3D-printed HA scaffolds with a Gyroid/TPMS porous structure via the VAT photopolymerization technology, *ii)* characterizing them in details from a physicochemical viewpoint by way of different complementary techniques, and *iii)* evaluating their *in vivo* performances in a large animal model (sheep) in comparison to the Bio-Oss® bovine bone substitute. The selection of the Gyroid structure among other TPMS was based on their high permeability and high stiffness compared to other TPMS scaffolds [62–64] makes them particularly well suited for bone regeneration [65]. The *in vivo* evaluation was multifold: the tissue effects were thoroughly investigated by macroscopic histology and semi-quantitative histopathologic observations while bone healing was evaluated both via an epifluorescence analysis using several fluorophores and by quantitative histomorphometry. In-depth comparative analyses are provided both at short (4 weeks) and long (26 weeks) time periods over this 6-months preclinical study, unveiling that this 3D-printed bioceramic scaffold with a trabecular-like structure at least equals the bone repair ability of the bovine bone-based standard, and even promoting earlier bone ingrowth. This pilot study is expected to fill the gap regarding the *in vivo* performances of Gyroid/TPMS trabecular-structured scaffolds in clinically-relevant conditions, so as to unlock further opportunities in maxillofacial, cranial and orthopedic surgeries with potential patient-specific 3D implant designs.

2. Materials and methods

2.1. Photopolymerizable slurry preparation

The general concept of VAT photopolymerization by Digital Light Processing (DLP) was used in this work, through the VAT approach aiming at curing a photopolymerizable slurry into a hardened resin under UV light. The starting photopolymerizable slurry was prepared in this work by adding stoichiometric hydroxyapatite (HA) powder up to 48 vol.% into a mix of dispersants, photo-initiators and acrylic monomers developed and commercialized by the 3D printing company CERHUM. The used slurry is referenced HAPM100T01 (CERHUM, Belgium). The combination of photoinitiator and dispersant used will be discussed in further details in an upcoming article work. The following acrylic monomers were used: *i)* diacrylate to favor linear polymerization despite low mechanical properties [66], *ii)* reactive tetraacrylate to enhance crosslinking for improving green parts mechanical resistance, and *iii)* pentaacrylates to promote general polymerization [67]. Trimethacrylate was also added to the resin to allow stronger links between subsequent layers during the process, thanks to its slow reactivity. The obtained mixture was then processed in a 3-roll mill to improve slurry homogeneity [51] before being used for printing.

2.2. 3D printing process

The TPMS design used in this work corresponds to a (double) Gyroid structure (Fig. 1) that can be described mathematically by the following equation [6]:

$$\left(\cos\left(2\pi/Lx\right)\sin\left(2\pi/Ly\right)+\cos\left(2\pi/Ly\right)\sin\left(2\pi/Lz\right)+\cos\left(2\pi/Lz\right)\sin\left(2\pi/Lx\right)\right)^2-t^2=0 \quad (1)$$

where L is the length of the pore cell, (x, y, z) are the spatial coordinates, and t is a parameter controlling the wall thickness of the TPMS cellular structure. In the present case, the value of t was set to 0.438. The pore size – described by the distance between two adjacent printing waves – was set to 900 µm (with a theoretical porosity of 72%) and the wall thickness was fixed to 200 µm.

The pieces, denoted MyBone® (CERHUM, Belgium), were printed using a Propmaker V6000 3D printer (Prodways, France) involving 2 doctor blades located next to 2 spreading rollers. The layers were cured at a wavelength of $\lambda = 365$ nm with a Digital Light Projector (DLP) using a resolution of 32 µm. The slurry was injected by way of a piston and spread onto the build platform. Before each layer, the build platform was lowered by 50 µm corresponding to one layer thickness. Resin polymerization under UV irradiation was performed as needed by the DLP projector in the designated areas following the STL file. These steps are repeated until a whole 3D scaffold is built. After printing the green body, it was cleaned from slurry residues and debinded to remove the photopolymerized resins, then sintered to densify the ceramic. In

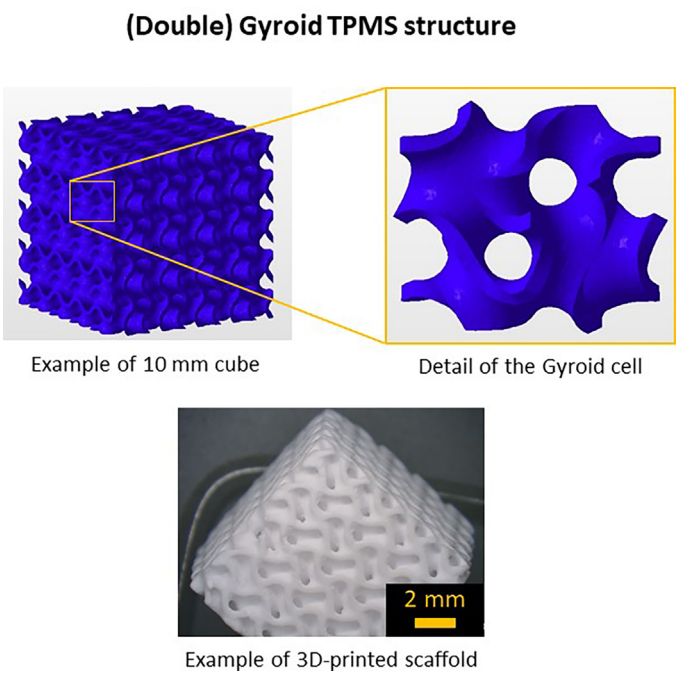

Fig. 1. Gyroid TPMS unit cell, lattice structure and example of 3D-printed scaffold.

this work, trials were carried out at different sintering temperatures (for a total duration of treatment of 90h), namely 1170 and 1270 °C, and the latter temperature was selected for the rest of the study including the animal testing.

2.3. Physicochemical characterization

X-ray diffraction (XRD) analyses were carried out to verify the apatitic structure of the 3D-printed scaffolds and compare to crystallographic features of the starting HA power and the Bio-Oss® reference. To this aim, XRD patterns were recorded with a Bruker D8 diffractometer (copper anticathode K_α, λ_{Cu} = 1.5418 Å) in the 2θ range 20–80° with a step of 0.02° for an acquisition time of 1 s.

Fourier transform Infrared (FTIR) spectra were also recorded, using the KBr pellet transmission methodology, to obtain complementary structural information. These analyses were run on a Nicolet IS50 spectrometer, in the 400-4000 cm^{-1} wavenumber range, with 64 scans of acquisition at a resolution of 4 cm^{-1}.

3D optical microscopy images were taken with a Hirox HRX01 microscope using a HR-5000E wide range ×20 objective. Additional microscopy analyses were carried out by Scanning Electron Microscopy (SEM) using a FEI/Philips XL30 ESEM FEG microscope. Samples were coated with platinum under vacuum with a JEOL JFC-1300 evaporating system prior to SEM observations.

To probe the percolation ability of the porous network, a gas permeability assay was operated in compressed air using a confining pressure of 4 bars to maintain the sample in position, and with an inlet percolating pressure of 1 bar. The pressure drop ΔP was set to 0.15 bar. The sample permeability k was then calculated via Darcy's law as follows [62,63]:

$$k = \frac{Q\mu L}{A\,\Delta P} \tag{2}$$

where Q is the fluid rate, μ is the dynamic viscosity of the fluid, L is the length of the sample and A the cross-section area of the sample. The value of permeability obtained (in m^2) is then a complex function of porosity, pore size, tortuosity and interconnectivity.

Solution impregnation of 3D-printed Gyroid scaffolds was also followed, in comparison to Bio-Oss®, using PBS as saline aqueous solution. Parallelepiped pieces of 10 × 10 × 20 mm^3 were simply contacted with the surface of the solution and the absorption rate was followed to assess the time (in seconds (") and hundreds of seconds) needed to reach full impregnation by capillarity.

Mechanical properties were investigated using an MTS-insight 10 SL machine through two types of tests, using a minimum of 10 replicates. Three-point bending assays were carried out to investigate global mechanical resistance features. The maximum flexural stress σ_f and strain ε_f prior to rupture were measured for 45 × 6 × 5 mm^3 specimens. The span was set to L = 38 mm (speed 0.5 mm/min). According to the ISO 178:2019 standard, σ_f and ε_f were determined as follows:

$$\sigma_f = \frac{3F_rL}{2wh^2} \tag{3}$$

$$\varepsilon_f = \frac{6s_rh}{L^2} \tag{4}$$

where F_r is the applied force at rupture (in Newton), L is the span of the test, s_r is the deflection distance at rupture, and w and h are respectively the width and thickness of the specimen.

To investigate more locally the mechanical resistance of the 3D-printed Gyroid scaffolds, macrospherical indentation measurements were made, as preconized by the ISO 13175-3:2012 standard for porous scaffolds (> 40% porosity). To this aim, cubic parts with a side dimension of 10 mm were analyzed using a 9.52 mm diameter spherical indenter at a crosshead speed of 0.5 mm/min. The loading direction was perpendicular to the printing direction.

2.4. In vivo testing

2.4.1. Animal model

Sheep was selected here as relevant animal model, recommended by the ISO 10993-6:2016 standard and identified for evaluating biomaterials intended for implantations in bone sites. This animal model was long used in intra-osseous implantation studies, which have been published in scientific peer-reviewed journals and is recognized by International Regulatory Organisms. In particular, the sheep femoral implantation site is highly standardized and associated with low rates of complication, where the lateral condyle of the sheep femur provides a cancellous bone site. In addition, the use of sheep femurs also allows implanting up to three implants per femur, thus increasing the number of sites per type of biomaterial without increasing the number of animals. The animal tests were carried out here, over *ca.* 6 months, in skeletally mature 2-3 y.o. female sheep, at the NAMSA center (Chasse-sur-Rhone, France), an AAALAC international accredited facility registered toward the French Department of Agriculture for animal housing, care and investigations.

2.4.2. Implantation methodology

The number of sites per type of biomaterial and animal used (10 per type of biomaterial and time-period for the test and control samples, 3 animals at least, respectively) was in keeping with the recommendation of the ISO 10993-6:2016 standard. Analysis time periods at 4 and 26 weeks were selected so as to evaluate the local tissue effects after short- and long-term implantation upon the consideration that the test biomaterial (made of stoichiometric HA) was considered to be non-resorbable due to a long degradation time. The 26-week time-period was assumed to be the duration where steady state was expected to be reached, characterized by the implant fully colonized by new tissue.

The 3D-printed synthetic ceramic scaffold addressed in this work (denominated MyBone® or "test" biomaterial in our *in vivo*

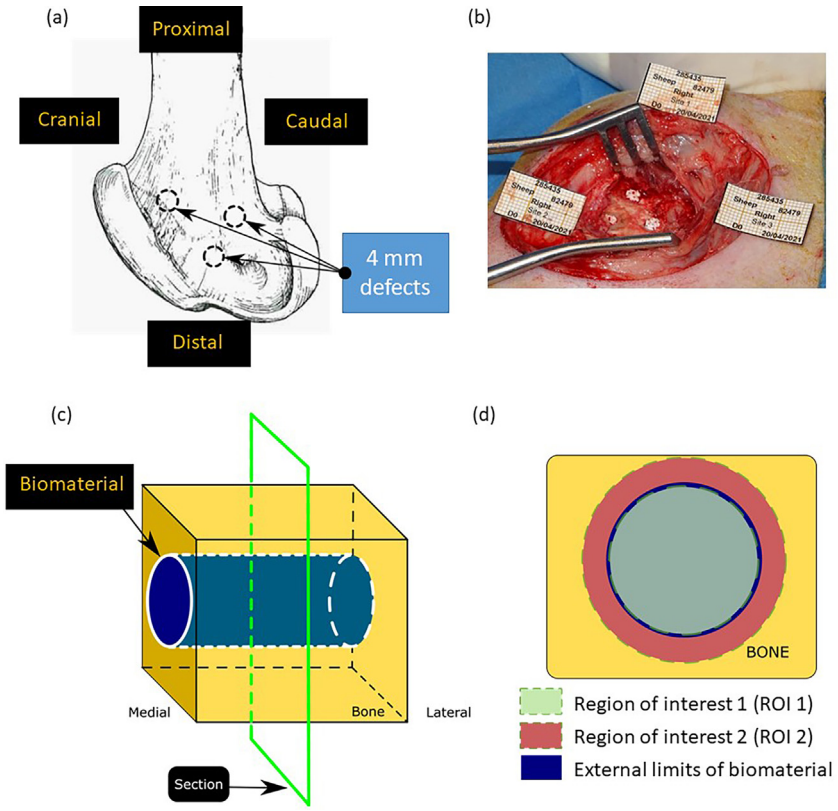

Fig. 2. (a) Schematic view of the medial aspect of a sheep right femoral condyle and of bone defects positioning, (b) example of surgical positioning of the tested biomaterial, (c) schematic of a cross section realized for the preparation of histological slides, (d) schematic of the positioning of regions of interest (ROIs) for the histomorphometry analysis.

results) was analyzed after 4 and 26 weeks of intra-osseous implantation, and compared to a control biomaterial consisting in a Bio-Oss® block (Geistlich Pharma France). Bio-Oss® is an anorganic bovine bone, used for example for more than 25 years as reference bone substitute in regenerative dentistry [13–19]. All implanted biomaterials, whether in the test or control groups, were in the form of cylinders of *ca.* 4 mm in diameter and 10 mm in length. All samples were sterile (steam sterilization at 134 °C for 18 min). Nine sheep (4 per time-period + 1 reserve animal) were bilaterally implanted in their medial femoral condyles with the test and control biomaterials. 3 bone defects were created in each medial femoral condyle ($n = 6$ sites per sheep). The test or control materials were inserted into premade defects according to the site allocation as shown on Fig. 2a,b.

Prior to the implantation, a small amount of autologous blood (about 1 mL per cylindrical material) was sampled from the animal. The collected blood was used to impregnate the material in a small surgical cup and to facilitate its insertion via a press-fit method. After the desired time point (e.g. 4 or 26 weeks after implantation), the designated animals were weighed and euthanized by intravenous injection of pentobarbital (Dolethal®, Vetoquinol).

2.4.3. Evaluation of local tissue effects

Tissue response (local tissue effects) was evaluated through several parameters: macroscopic qualitative observations, qualitative and semi-quantitative histopathological evaluations, and Reactivity Ranking (RR) assessment.

a) Histologic preparation

For the histology slides preparation, the following customary reactants were used: 10% (v/v) neutral buffered formalin (NBF, VWR), xylene, ethanol, methyl methacrylate. The implantation sites were harvested and fixed in 10% NBF. After complete fixation in 10% NBF, implanted sites were dehydrated in alcohol solutions of increasing concentration, cleared in xylene and embedded in polymethylmetacrylate (PMMA) resin. X-ray radiography from the embedded explants were taken. The orientation of the cutting plan was determined based on the X-ray imaging. A transverse section was created in the upper half according to the radiography (Fig. 2c). The PMMA resin block was cut and opened and not grinded down in order to preserve the cortical structure. The sections were obtained by a microcutting and grinding technique (Exakt®, approximately 40 μm thickness). The sections were stained with modified Paragon (toluidine blue-basic fuchsin) for qualitative and semi-quantitative analysis of new bone formation and inflammatory reaction. Paragon allows differentiation between preexisting bone, new bone and bone substitute material [68]. An additional serial section was created for epifluorescence analysis that was not stained.

In addition, the draining lymph nodes (popliteal lymph nodes, 2 per animal) were macroscopically examined, sampled and fixed in 10% NBF.

b) Histopathology evaluation

The histopathologic qualitative and semi-quantitative analyses of the implantation sites were conducted in accordance with the OECD Good Laboratory Practice regulations, ENV/MC/CHEM (98) 17 and with the United States Food and Drug Administration Good Laboratory Practice regulations, 21 CFR 58. Qualitative and semi-quantitative histopathologic evaluation of the local tissue effects at the implantation sites were conducted according to the standard

Table 1
Fluorescent labelling strategy (time points).

Fluorochrome	4-week group	26-week group
Calcein Green (CG)	Day 7	Week 16
Xylenol Orange (XO)	Day 14	Week 20
Oxytetracycline (OTC)	Day 21	Week 24

(ISO 10993 - Part 6). Representative photomicrographs were taken of the areas of interest.

c) Reactivity Ranking (RR) determination

Based on Annex E of standard ISO 10993-6:2016, the Reactivity Ranking (RR) was evaluated in two steps. In a first step, the total score of each test and control material was calculated from the histopathologic semi-quantitative analysis. It corresponded to the sum of the tissue damage and cellular inflammatory parameter scores weighted with a factor 2 plus the repair phase of inflammation and osteolysis parameter scores (total score of each test/control site = 2 × tissue damage and cellular inflammatory parameters + repair phase of inflammation and osteolysis parameters). In a second step, the value of RR reflecting the local tissue effects was determined by subtracting the average score of the control from the average score of each test material. The RR was calculated based on the average scores before being rounded-off to the nearest 0.1. A negative difference was recorded as zero. The reaction to the test material was graded as minimal or no reaction (0.0 to 2.9), slight reaction (3.0 to 8.9), moderate reaction (9.0 to 15.0) or severe reaction (> 15.1).

2.4.4. Evaluation of bone healing response

Bone healing performances were assessed thanks to epifluorescence analyses after fluorochromes labeling and through a quantitative histomorphometry analysis.

a) Fluorochrome markers preparation for epifluorescence follow-up

The epifluorescence analysis allowed us to follow the progress in bone formation – newly formed calcified tissue lines seen as mineralization fronts – around and within the biomaterials for unstained resin sections. To this aim, multiple staining was achieved. oxytetracycline (OTC, Terramycine® LA, Zoetis France), xylenol orange (XO, Sigma) with final concentration 9% and calcein green (CG, Sigma) with final concentration 3% were injected intramuscularly during the living phase of the animal, at different time points to follow the mineralization kinetics (Table 1).

b) Histomorphometry

The histomorphometric analyses were conducted on all the sections stained with modified Paragon. Sections were digitalized using a scanner (Zeiss AXIOSCAN Z1) in a bright field setup and analyzed with a color image system (Tribvn, France, CALOPIX 3.2.0). For each site, two standardized Regions of Interest (ROIs) were defined as a circle having the diameter of the initial defect (4 mm), referred to as ROI 1 (inner), and a 1 mm width external corona circle defined as ROI 2 (outer) as displayed in Fig. 2d. Quantitative histomorphometric data were obtained in percentage corresponding to the proportions of ROI surface occupied by the different components (bone tissue, bone marrow, fibrous tissue, implant). The bone-to-implant (BIC) contact was determined as the percentage of the sample perimeter in direct contact with the mineralized bone tissue, and the total mineral content (TMC) was also calculated by considering both the mineralized structure (implant and bone).

2.4.5. Ethical considerations

This study was conducted in accordance with the OECD Good Laboratory Practice regulation ENV/MC/CHEM (98) 17 and with the United States Food and Drug Administration Good Laboratory Practice regulation 21 CFR 58. The NAMSA Ethical Committee provided project authorization via the reference number APAFIS#23401-2017050517312149 v5. The animal housing was undergone under controlled room temperature and relative humidity recorded daily (temperature range 15-24 °C). The light cycles were controlled using an automatic timer (12 hours of light, 12 hours of dark). After the immediate and scheduled post-operative period (approximately 5 weeks) and in agreement with a veterinarian, the sheep were housed in a farm setting (*Bergerie de la Combe aux Loups*, France) conforming to the European requirements (Directive EU/2010/63), where temperature and humidity were not controlled. The farm provided ISO 9001 certified facilities.

2.4. Statistical methods

Statistical analyses (5% risk, $p = 0.05$) on each individual response were conducted using the SPSS software (24.0, SPSS Inc.). Data expressed as mean ± standard deviation were then statistically compared between the test and the control groups via a One Way Analysis of Variance (ANOVA) with a 5% risk ($p = 0.05$) using the same software.

3. Results and discussion

3.1. HA scaffolds with 3D-Printed TPMS structure

With the view to obtain HA porous scaffolds with high permeability that fulfill all porosity criteria recommended by literature, a Triply Periodic Minimal Surface (TPMS) structure with the Gyroid geometry was investigated in this work, so as to exhibit both a high porous network (continuous tortuosity of highly interconnected pores) and appropriate mechanical properties (reduced stress concentration). The 3D scaffolds were printed by DLP using the VAT strategy via selected area-induced UV irradiation of a photopolymerizable resin containing 48 vol. % of HA powder, as indicated in the experimental section. After printing the green body, the pieces were debinded and densified, either at 1170 °C or 1270 °C over a total treatment duration of 90h.

Fig. 3 reports the obtained porous scaffolds observed by 3D optical microscopy and SEM, evidencing the successful formation of a Gyroid structure, as planned, and the repetitive motif can be seen throughout the printed pieces. The experimental wall thickness (e_{wall}) was measured from the 3D optical microscopy images by considering a pool of $n = 48$ measurements, leading to $e_{wall} = 256 \pm 25$ µm (Supplementary Information, Fig. S1). This value agrees well with that measured by SEM in Fig. 3d and remains close to the theoretical value of 200 µm, in keeping with the 32 µm resolution of the Digital Light Projector used and with the slight possible diffusion of the UV light during the process. The pore size – defined as the distance between two adjacent parallel printed waves – was also found to approach the theoretical 900 µm as seen by SEM (Fig. 3d). Greater magnification (Fig. 3f) allows visualizing the high densification state of the HA particles that constitute the pore walls and ensure their mechanical stability: the starting spherical morphology of the HA powder (Fig. S2) is still visible but the particle have clearly undergone massive sintering with the creation of grain boundaries of molten-like appearance (Fig. 3c,f).

The porous volume was evaluated from geometrical measurements of parallelepiped pieces (10 × 10 × 10 mm^3) based on their mass and theoretical density (3.16 g/cm^3 for HA). Whether using a calcination temperature of 1170 or 1270 °C, a cumulated porous

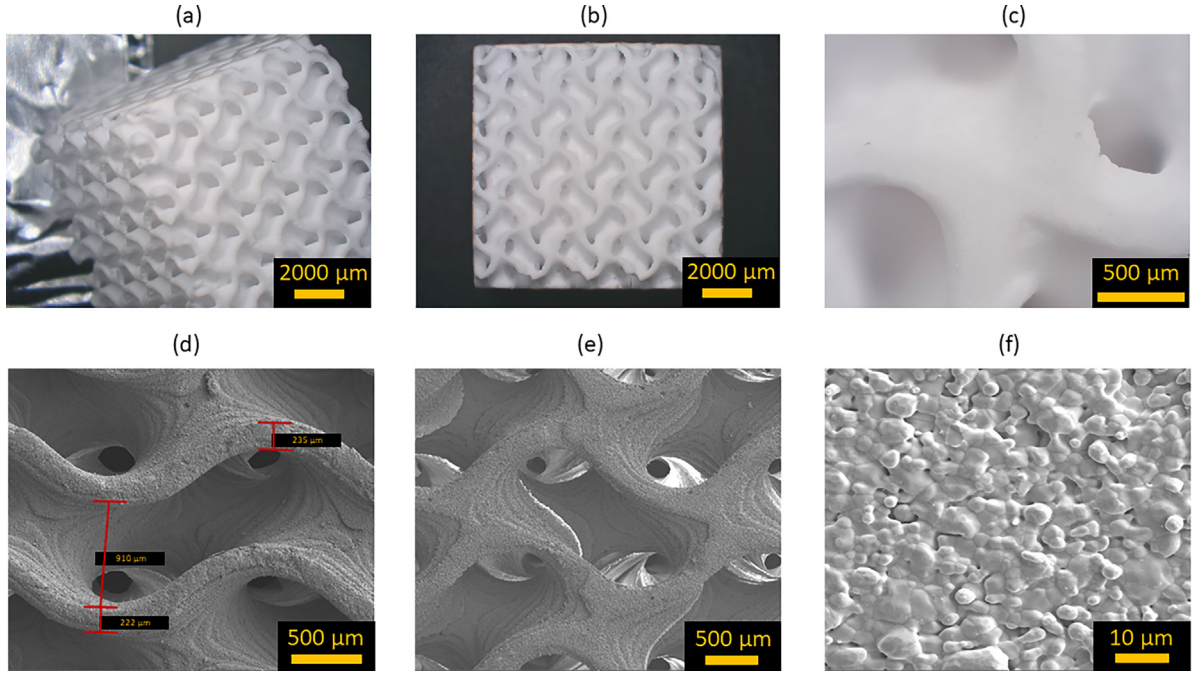

Fig. 3. (a) to (c): 3D optical microscopy images of the Gyroid design obtained for the HA scaffolds prepared in this work (sintering temperature: 1270 °C), (d) to (f): SEM micrographs of structural details.

volume of 64.0-64.5% was systematically obtained (Table S1), and this value did not change either after sterilization. This value is slightly lower than the expected theoretical 72% set by the STL file, which may be explained by slight variations in the wall thickness, as mentioned above relating to the 32 µm resolution of the DLP. Indeed, recalculation of the theoretical porous volume starting from parameters, in the STL file, of 910 µm as pore size and 256 µm as wall thickness led to 66.9%, thus very close to the experimental values. The > 64% porous volume however allows expecting a high percolating potential for such TPMS structures, and especially with a low friction coefficient thanks to the Gyroid geometry. In parallel, the true density of the HA skeleton constituting the 3D-printed pieces was determined from fully dense pieces, reaching 2.86 ± 0.03 g/cm^3 and pointing to a densification rate of 90.5% (for sintering at 1270 °C). These findings appear in good agreement with the densified microstructure observed by SEM in Fig. 3c,f.

In order to give a quantitative assessment of the openness of the porous network, gas permeation assays were carried out using compressed air. This assay allows following the capacity of a fluid to pass through a confined porous sample upon a pressure gradient [69]. The order of magnitude of k is directly dependent on the pore structure, pore size, and interconnectivity [70]. The measured gas permeability k was here higher than 9.36 × 10^{-12} m^2 (i.e. the limit of the equipment). A large span of values ranging typically from 10^{-15} to 10^{-9} m^2 were reported in the literature for various porous systems including for bone tissue engineering (e.g. [70]). The value found here is close to those obtained for example for calcium carbonate, PCL or electrospun fibrinogen scaffolds [70]. Taking into account the final use of these 3D-printed pieces surrounded by body fluids *in vivo*, we have also performed dynamic impregnation tests in PBS solution. This assay was carried out both with a Gyroid-structured 3D-printed piece and with a Bio-Oss® scaffold, on parallelepiped pieces of 10 × 10 × 20 mm. Results, shown in Fig. 4, showed the high water absorption power of the printed Gyroid scaffold, reaching full impregnation at 0"44 for the Gyroid. In comparison, the Bio-Oss® reference reached total impregnation at 1"28. These findings demonstrate the high percolating/absorptive character of the Gyroid porous network, and also point out the high hydrophilicity of this scaffold, which is an important factor in view of the implantation.

X-Ray Diffraction (XRD) analyses were carried out before and after printing/calcination at 1270 °C, to check for any possible structural modifications and to confirm the phases in presence. The obtained patterns showed the absence of detectable crystallographic modification of the hydroxyapatite phase, as illustrated in Fig. 5a. As expected, the characteristic diffraction lines of HA (with reference to the PDF file # 09-0432) are clearly identifiable with no secondary peaks, and the printing and calcination processing steps did not alter the HA phase. For the sake of comparison, the XRD pattern of the bovine bone-derived standard Bio-Oss® has also been added in the fig., where the typical (low crystallinity) apatitic phase constituting the mineral part of bones can be identified. These findings were complemented by FTIR analyses (Fig. 5b): the obtained IR spectra evidenced again the characteristic apatitic features in all samples studied, with not detectable modification of the HA phase due to the printing or calcination steps. For the Bio-Oss® sample, additional vibration bands from carbonate groups are also visible, as indicators of the carbonation of the apatite phase in bone. These XRD and FTIR data thus validate the process and the apatitic nature TPMS Gyroid 3D-printed pieces obtained in this work, with not alteration inferred by the process itself.

The 3D-printed Gyroid scaffolds prepared in this work (sintered at 1270 °C) are intended to be implanted in bone sites. Therefore, they should exhibit mechanical strength sufficient to be handled by the surgical team and potentially re-cut for dimension adjustments to fit the bone defect to be filled. Also, the scaffold should be able to undergo some degrees of mechanical shocks due to movements and potential transient collisions. Mechanical assessments have thus been carried out to examine and quantify the ability of these 3D-printed porous scaffolds (~65% porosity) to endure such solicitations. Three-point bending tests were realized to determine the maximum flexural stress σ_f and strain ε_f prior to rupture, leading to mean values of $\sigma_M \cong 7$ MPa and $\varepsilon_M = 0.15\%$ (see an example test in Fig. 6a). These values are relevant for the applications envisioned here [71,72].

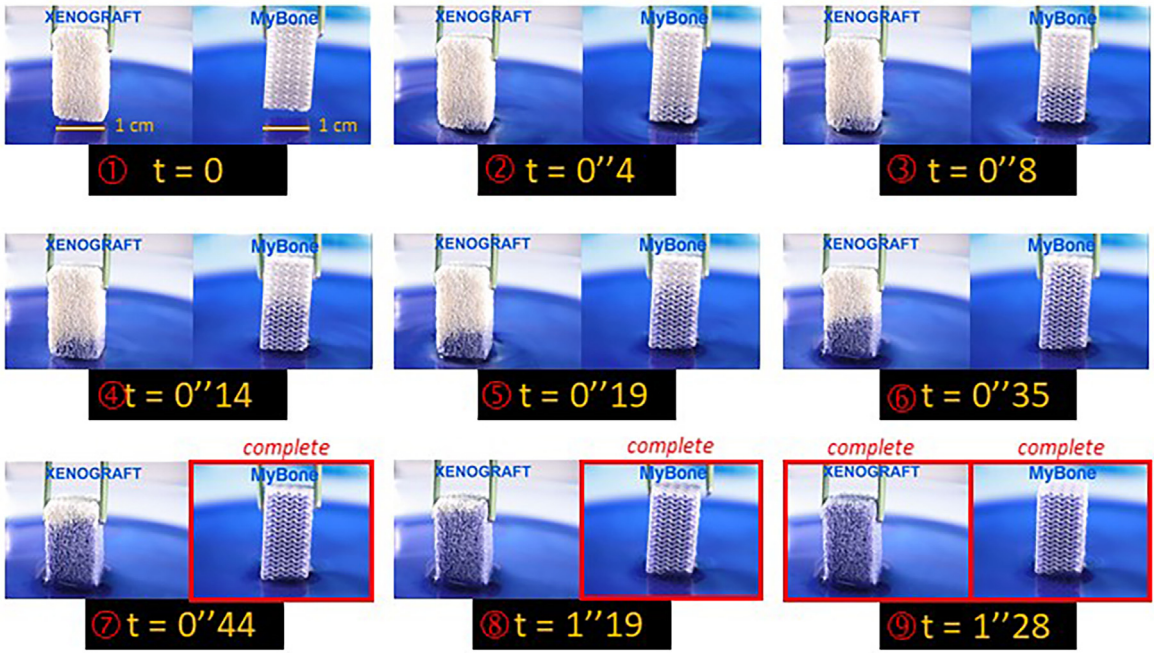

Fig. 4. Test of impregnation of the TPMS Gryoid sample (denoted "MyBone®") in PBS solution, compared to Bio-Oss® bovine reference (denoted "Xenograft") versus time. Total absorption, marked by the red squares, was reached at 0"44 for the Gyroid compared to 1"28 for Bio-Oss®.

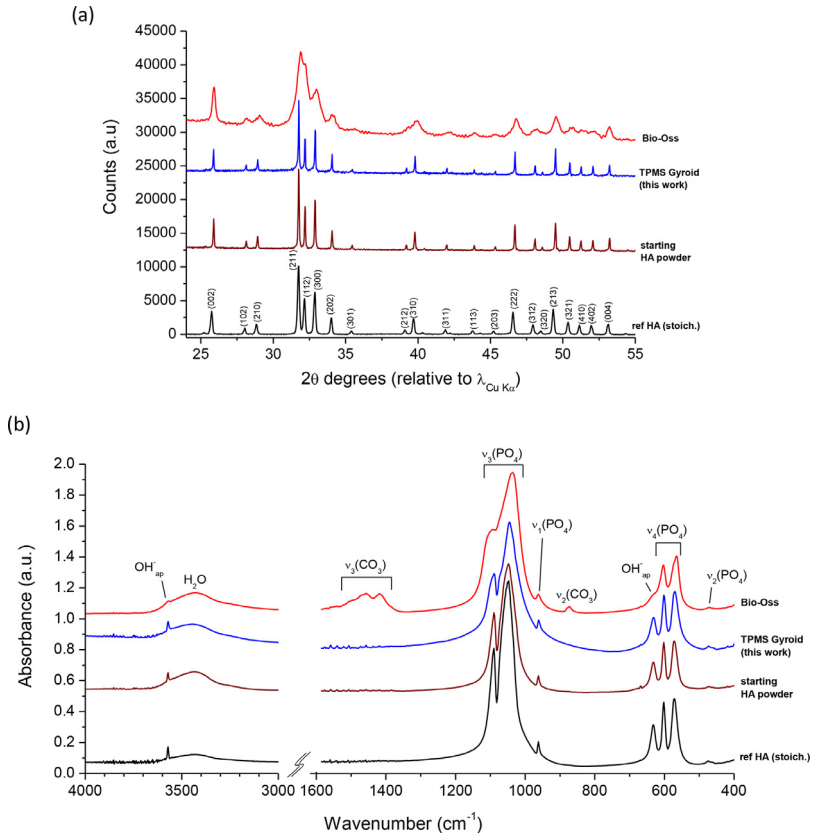

Fig. 5. (a) XRD patterns and (b) FTIR spectra before and after 3D printing, as well as for the Bio-Oss® bovine-derived reference and reference stoichiometric hydroxyapatite.

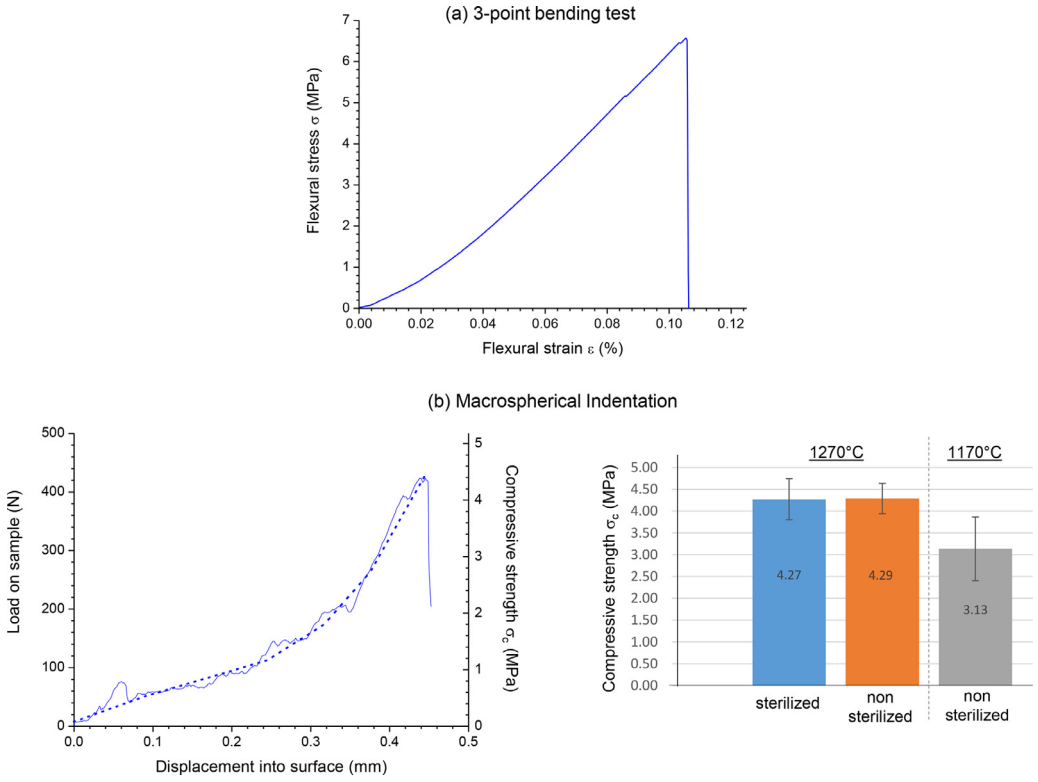

Fig. 6. (a) 3-point bending tests and (b) macrospherical indentation on 3D-printed TPMS scaffolds with Gyroid porous structure prepared in this work.

While 3-point bending tests refer to global mechanical properties, more local assays were also performed to complete the study, through macrospherical indentation measurements [73] which are preconized by the ISO 13175-3:2012 standard for porous CaP scaffolds (> 40% porosity). The maximal compressive strength σ_c is provided as an indicative value and is calculated without taking into account the porosity of the material. It reached a mean value (over 11 replicates) of $\sigma_c = 4.29 \pm 0.35$ MPa, corresponding to an applied force of $F = 421 \pm 34$ N (Fig. 6b). Again, these values are consistent with the surgical implantation applications aimed in bone sites. Importantly, similar values were reached for sterilized samples ($\sigma_c = 4.27 \pm 0.47$ MPa, $F = 417 \pm 46$ N) showing no impact of the sterilization process on the mechanical properties of the 3D-printed pieces. It may on the contrary be worth noting that 3D pieces sintered at 1170 °C instead of 1270 °C led to significantly lowered maximal compressive strength ($\sigma_c = 3.13 \pm 0.73$ MPa). Since we showed above that the total porous volume essentially remained unchanged for pieces sintered at 1170 °C or 1270 °C, these indentation measurements unveil the direct impact of the densification rate on the final mechanical resistance of the 3D-printed scaffolds. At this point, it should be noted however that these indentation measurements were performed by following the crosshead displacement which may not be as precisely reached as using strain gauge or optical techniques (not available on the setup used here) – although especially appropriate for characterizing dense specimens. Yet, the main objective of the mechanical tests run in this study was to obtain indicative measurements of the compressive strength of Gyroid structures, rather than focusing on other parameters such as Young's modulus or deformation of these scaffolds. The tested specimens were indeed highly porous structures with a porosity of 66%. As determined through the flexural tests, the observed deformation was minimal, approximately 0.113%, influenced by the relatively higher deflection due to the presence of porosity in the samples. While the use of strain gauges or optical techniques could have potentially yielded more precise results, the current findings show strong coherence among the mechanical data, and the inclusion of such techniques would not have significantly modified the outcomes.

The effect of the sintering temperature on the HA microstructure has been further analyzed by SEM, between these two limit temperatures. As may be seen in Fig. 7, a clear densification trend is visible when increasing the temperature, and a minimum temperature of 1200 °C appears necessary to avoid the detection of non cohesive HA particles. Considering these conclusions, the Gyroid structure sintered at 1270 °C has been selected for the *in vivo* evaluations reported below.

Although these results fall within the magnitude of mechanical strength of trabecular bone, they are relatively low. This is attributed to the testing method used (macrospherical indentation), which yields lower results compared to uniaxial compression in addition to the intrinsic low strength of hydroxyapatite. One possible solution to further enhance the mechanical resistance of this type of substitute is to incorporate a dense contour, as demonstrated by Charbonnier et al. [53]. Another approach would involve introducing Gyroid gradients to increase the mechanical strength by integrating less porous Gyroids at the periphery of the substitute to mimic cortical bone [74]. A combination of these two solutions would enable a smoother transition between the dense contour and the highly porous Gyroids at the center.

3.2. *In vivo* testing

The high biocompatibility *in vitro* and *in vivo* (rat) of such 3D-printed Gyroid structures has been explored in a preceding paper [75]. In the present work, we have evaluated *in vivo* in a large clinically-relevant animal model the properties of these 3D scaffolds (test group) through intra-osseous implantations in the sheep. Analyses were carried out at two relevant time points, namely 4 and 26 weeks after surgery. A sharp statistical follow-up was undergone based on several qualitative and quantitative

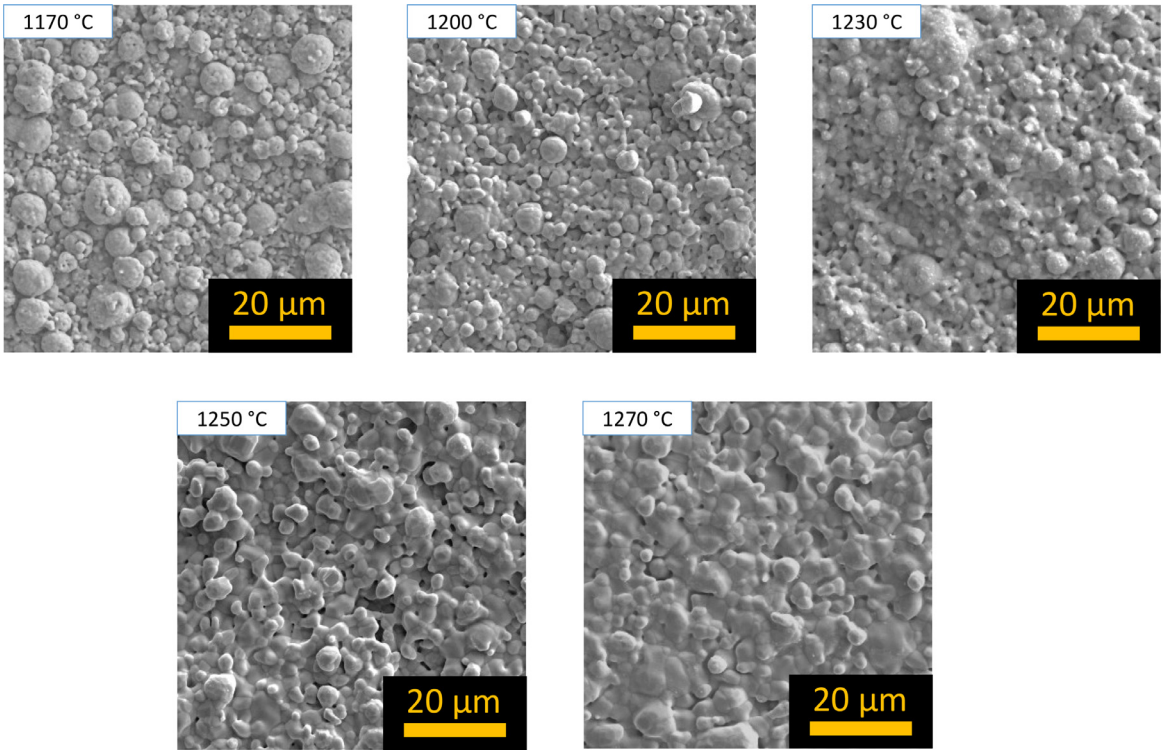

Fig. 7. SEM observations on the effect of the sintering temperature on HA morphology.

assessments to examine both the local tissue response and the bone healing performance. To this aim, comparison was made all along the study with an internationally acknowledged reference standard, Bio-Oss®, an anorganic bovine bone (control group). Indeed, Bio-Oss® has been used for decades as a reference standard in bone surgery. It has for instance become the reference of choice in regenerative dentistry and was shown to exhibit excellent osteoconductive properties [17–19] with a high osteointegration capacity [13–16].

No adverse event occurred whatsoever, whether with the test or the control groups, during the whole surgical procedure nor during the in-life phase of the study. The follow-up of individual body weights did not evidence any detrimental effect of the materials. At week 26, all the sheep gained weight (Table S2).

Macroscopic observations of histology slides corresponding to 4 and 26 weeks did not show any abnormal inflammatory reaction around the implantation sites. Also, no abnormal findings were observed on the popliteal lymph nodes. These findings thus depict the absence of detectable signs of toxicity on macroscopic analyses.

Histopathological evaluations were made to investigate further the tissue response to the implanted materials, down to smaller scales. Representative micrographs at 4 and 26 weeks are presented in Fig. 8, and the summary of the semi-quantitative histopathologic analysis is reported in Table 2. Several parameters were followed in this study, including the presence of cells such as macrophages, lymphocytes and multinuclear cells, signs of necrosis or fibrosis, hemorrhage and tissue degeneration markers. All of these parameters were found to remain similar among the test and the control groups, and in particular no adverse effect was detected whatsoever for the tested biomaterial. The bone-forming ability of the materials was also examined based on the assessment of the extent of bone remodeling and mineralization. At 4 weeks, the test group was slightly more osteointegrated than the control but the extent of bone ingrowth by osteoconduction was similar. The woven bone penetrating the two materials harbored more bone marrow in the test material than in the control group, which reflected higher signs of bony maturation in the test group. At 26 weeks, again the test biomaterial was slightly more osteointegrated than the control but the extent of bone ingrowth by osteoconduction appeared slightly lower. Overall, the tissue response of the tested biomaterial was found to be very close to the one obtained with the Bio-Oss® bovine reference.

The general reactivity ranking (RR) score (Table 2) was calculated on the basis of the detailed scoring methodology based on the ISO 10993-6 and described in Table S3, and using the related numerical data of the various parameters considered (Table S4). Four main types of parameters have been taken into account in the scoring:

(1) Tissue damage and cellular inflammatory parameters (including observation giant cells, lymphocytes and necrosis signs among other parameters);
(2) Repair phase of inflammation and osteolysis. This includes signs of neovascularization, osteolysis, and fibrosis (ultimate inflammatory stage characterized in histology by an organized deposit of mature collagen);
(3) Bone healing parameters. Besides observation of osteoblastic cells, this includes:
   - Osteointegration: process whereby no reactive tissues create a barrier between host tissues and a biomaterial, resulting in perfect continuity between the native tissue and the tissue colonizing the biomaterial.
   - Bone mineralization: analyzed by epifluorescence microscopy. Bone fluorescent markers assess the mineralized bone at the successive injection times of fluorescent markers (assessed on unstained resin slides).
   - Bone neoformation: amount of bone growing inside the biomaterials.

Table 2
Summary of the semi-quantitative histopathologic analysis. T stands for the tested Gyroid biomaterial, C stand for the control Bio-Oss® scaffolds. W4 and W26 respectively stand for observations made at 4 and 26 weeks.

Time period	Group		Macrophages	Lymphocytes	Plasma cells	Polymorphonuclear cells	Giant cells/Osteoclasts	Necrosis	Fibrosis	Neovascularization	Osteolysis	Fibrin	Hemorrhage	Cell or tissue degeneration	Fibroplasia	Bone Marrow	Encapsulation	Osteoblastic cells	Bone formation	Osteoconduction	Osseointegration	Bone remodelling (compared to distant normal bone density)	Bone mineralization (CG)	Bone mineralization (XO)	Bone mineralization (OTC)
W4	C (n=10)	Mean	1.0	1.1	0.1	0.0	0.9	0.0	2.7	2.2	0.0	0.0	0.6	0.0	1.1	1.0	0.0	2.4	1.8	2.2	3.2	0.0	1.1	1.8	2.2
		SD	*0.0*	*0.3*	*0.3*	*0.0*	*0.3*	*0.0*	*0.5*	*0.4*	*0.0*	*0.0*	*0.5*	*0.0*	*0.3*	*0.8*	*0.0*	*0.7*	*0.6*	*0.6*	*0.9*	*0.0*	*0.3*	*0.4*	*0.4*
	T (n=10)	Mean	1.0	0.5	0.1	0.1	1.0	0.0	1.9	2.1	0.3	0.0	0.8	0.0	1.2	2.1	0.0	2.3	2.2	2.3	3.7	0.0	1.2	2.2	2.0
		SD	*0.0*	*0.5*	*0.3*	*0.3*	*0.0*	*0.0*	*0.7*	*0.3*	*0.5*	*0.0*	*0.4*	*0.0*	*0.6*	*0.8*	*0.0*	*0.5*	*0.6*	*0.5*	*0.5*	*0.0*	*0.4*	*0.4*	*0.0*
W26	C (n=10)	Mean	1.0	0.1	0.0	0.0	0.2	0.0	0.4	1.0	0.3	0.0	0.0	0.0	0.0	2.7	0.0	1.0	3.3	3.3	3.7	2.8	1.7	1.2	1.0
		SD	*0.0*	*0.3*	*0.0*	*0.0*	*0.4*	*0.0*	*0.5*	*0.0*	*0.5*	*0.0*	*0.0*	*0.0*	*0.0*	*0.5*	*0.0*	*0.6*	*0.6*	*0.5*	*0.5*	*0.4*	*0.5*	*0.4*	*0.6*
	T (n=10)	Mean	1.4	0.2	0.0	0.0	0.3	0.0	0.7	1.0	0.7	0.0	0.0	0.0	0.0	2.9	0.0	0.6	2.7	2.8	3.9	3.0	1.0	1.0	0.7
		SD	*0.5*	*0.4*	*0.0*	*0.0*	*0.5*	*0.0*	*0.6*	*0.0*	*0.5*	*0.0*	*0.0*	*0.0*	*0.0*	*0.3*	*0.0*	*0.5*	*0.6*	*0.4*	*0.3*	*0.0*	*0.0*	*0.0*	*0.5*

Time Period	Group	Average score	Reactivity Ranking	Reaction
W4	C	11.1	NA	NA
	T	9.7	0	**null to minimal**
W26	C	4.3	NA	NA
	T	6.2	1.9	**null to minimal**

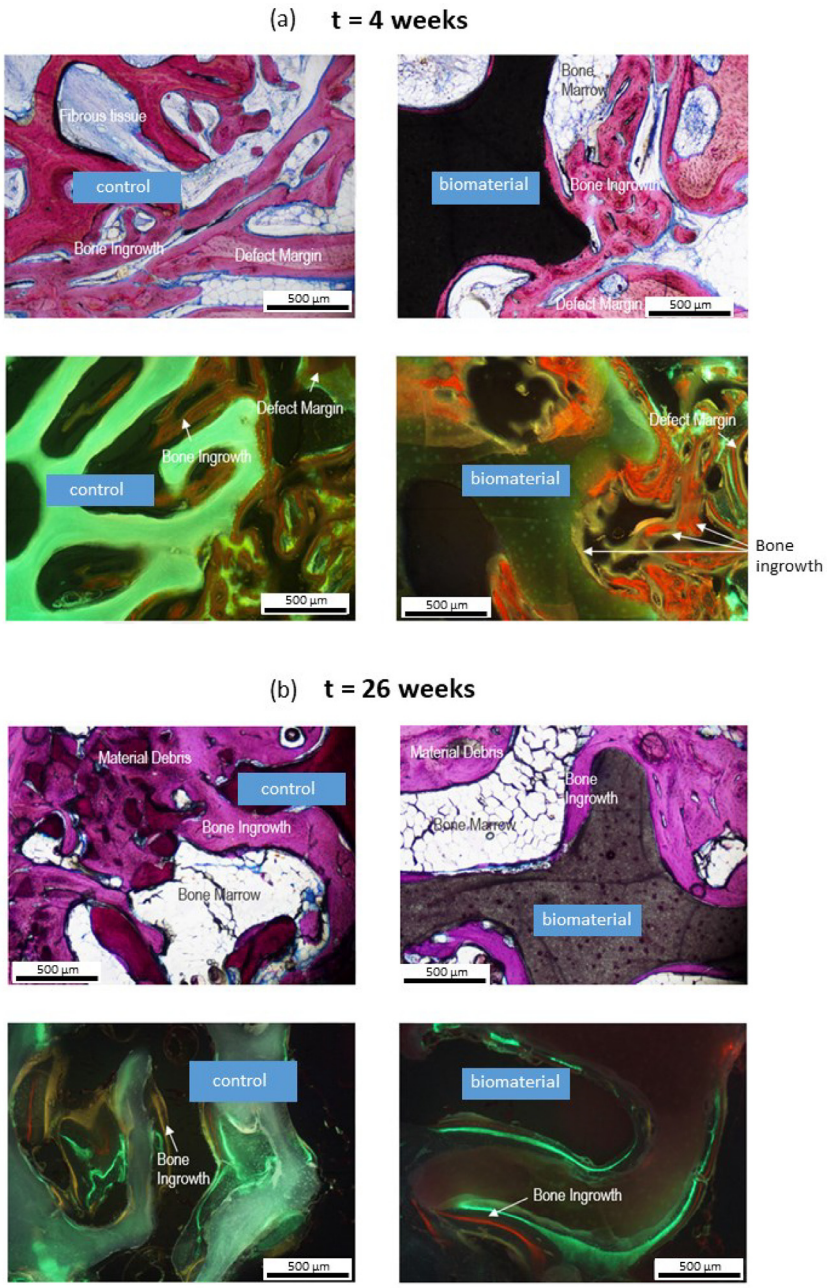

Fig. 8. Representative micrographs of histopathological evaluations to the implanted materials, at 4 weeks (a) and 26 weeks (b). Bone fluorochrome markings: Calcein Green (green lines), Xylenol Orange (orange lines), Oxytetracycline (yellow lines).

- Osteoconduction: extent of bone lining the inner and outer surface of the biomaterial.
- Bone remodeling (compared to distant normal bone density);

(4) Further parameters including:

- Fibroplasia: normal wound healing phenomenon characterized in histology by the presence of an edematous tissue where the orientation of newly formed vessels appears orthogonal to the orientation of early fibrous tissue deposition. This stage is transitory and corresponds to early collagen deposition. The accuracy of the scoring of this parameter could be improved using a modified Masson's Trichrome stain.
- Encapsulation: concentric organization of mature collagen deposits that tend to isolate the biomaterial from the host tissues.

At both 4 and 26 weeks, as per ISO 10993-6, the test biomaterial elicited a null to minimal reaction, as could be expected from all of the above results indicative of the non-toxic and high osteointegration properties evidenced.

The bone healing properties of the biomaterial were then more specifically evaluated through a bone dynamics analysis using polyfluorochromes. The newly formed calcified tissue lines (mineralization fronts) were indeed evaluated by epifluorescence microscopy. To this end, Oxytetracycline, Xylenol Orange and Calcein Green were injected intramuscularly during the living phase of the animal and at different relevant time points to follow the mineralization kinetics. The fluorochrome strategy is presented in Table 1. No signs of bone apposition were significantly visible at day 7 (D7) in either group, but from D14 sequential appositional mineralization occurred with a slightly higher expression in the test group. The bone dynamics analysis (polyfluorochromes) showed – at the

Table 3
Summary of quantitative results of histomorphometry at 4 and 26 weeks, for regions of interest ROI 1 « in » and ROI 2 « out ».

Time period	ROI	Group/Article		BIC (%)	Bone Area (%)	Implant Area (%)	TMC (%)	Fibrous Area (%)	Bone marrow area (%)
4W	ROI in	C	Mean	50.9$^{(26W)}$	21.1$^{(26W)}$	33.9 $^{(T)\ (26W)}$	55.0$^{(T)\ (26W)}$	37.2$^{(T)\ (26W)}$	7.8$^{(26W)}$
		(n=10)	*SD*	*16.0*	*5.6*	*5.2*	*9.9*	*9.5*	*12.2*
		T	Mean	60.3	20.8	45.9$^{(C)}$	66.6$^{(C)\ (26W)}$	18.4$^{(C)\ (26W)}$	14.9
		(n=10)	*SD*	*12.1*	*7.8*	*5.1*	*4.2*	*8.4*	*10.6*
26W	ROI in	C	Mean	73.1$^{(4W)}$	45.3$^{(T)\ (4W)}$	25.2$^{(T)\ (4W)}$	70.5$^{(4W)}$	4.0$^{(4W)}$	25.4$^{(4W)}$
		(n=10)	*SD*	*10.6*	*11.3*	*7.8*	*10.1*	*1.8*	*10.9*
		T	Mean	71.0	27.0$^{(C)}$	47.3$^{(C)}$	74.3$^{(4W)}$	3.3$^{(4W)}$	22.4
		(n=10)	*SD*	*11.4*	*6.9*	*3.0*	*6.6*	*1.7*	*6.3*

Time period	ROI	Group/Article		Bone Area (%)	Fibrous Area (%)	Bone marrow area (%)
4W	ROI out	C	Mean	46.4	5.1$^{(26W)}$	48.4
		(n=10)	*SD*	*19.9*	*2.2*	*21.0*
		T	Mean	42.9	3.4$^{(26W)}$	53.7
		(n=10)	*SD*	*17.3*	*1.5*	*17.3*
26W	ROI out	C	Mean	41.8	0.5$^{(4W)}$	57.7
		(n=10)	*SD*	*12.3*	*0.3*	*12.2*
		T	Mean	45.7	0.6$^{(4W)}$	53.7
		(n=10)	*SD*	*17.4*	*0.4*	*17.3*

$^{(T, C, time):}$ significant difference with the corresponding group.

exception of the control group at week 16 pointing to a slight to moderate marking – that the mineralization activity slowed down in the two groups from week 16 to week 24 post-implantation. This was consistent with normal bone remodeling phase.

In order to complement this study, the bone healing performance of the 3D scaffold engineered in this work was additionally assessed via quantitative histomorphometric analyses. To this aim, several measures were taken within each Region of Interest (ROI) defined in the Materials and Methods section (Fig. 2b), and corresponding to “inner” and “outer” domains at the site of implantation. The bone-to-implant (BIC) contact was in particular defined by the percentage of the sample perimeter in direct contact with the mineralized bone tissue. Then, the percentages of each ROI surface occupied by either bone tissue, bone marrow (lacunae), fibrous tissue or the implant itself were determined. Finally, the total mineral content (TMC) was calculated from the sum of mineralized structures (implant + bone). The quantitative results of this histomorphometry analysis are summarized in Table 3.

At 4 weeks, the test biomaterial occupied a significantly larger space than in the control, leaving then smaller space for bone ingrowth in the test group. However, at the early stage of implantation, the bone area density and the BIC values did not significantly differ between the two groups. More than 50% of the material surface in ROI 1 “in” was in direct contact with the newly formed bone (osteointegration) in the two groups. In ROI 2 “out”, around the defect the bone, fibrous and bone marrow densities did not significantly differ between the two groups. When considering the TMC, a significantly higher density value was obtained in the test group with respect to the control. Also, the fibrous tissue generated in the test group was significantly lower compared to the control. Concerning the bone marrow produced, no significant difference was established between the two groups, although the average density value in the test group was higher, which was in agreement with the qualitative histopathological findings reported above. Generation of bone marrow accompanying bone ingrowth was viewed as a favorable pattern of bone formation, because this feature was close to the physiological bone healing process. At 26 weeks, a faster material degradation occurred in the control group resulting in a significant diminution of the control area density from 4 to 26 weeks. No significant drop of the test area density was evidenced despite the few signs of material degradation qualitatively observed on histopathology. Higher bone area density was noted in the control group due to the faster degradation rate leading to more space in the defect for bone ingrowth. Still, the BIC and the TMC values did not significantly differ between the two groups at 26 weeks. The fibrous tissue significantly dropped in the two groups to reach low and similar values ($< 5\%$) at this time point. The TMC value significantly increased in the two groups at 26 weeks, with no significant difference. Even though the bone ingrowth was significantly higher in the control group, the value of the osteointegration did not differ in the two groups, pointing out the noticeable osteoconductive property of the Gyroid scaffold.

Therefore, as for the tissue response data obtained by histopathological assessments, the bone dynamics analysis and the histomorphometry quantifications show that the 3D porous biomaterial tested in this study achieves very similar performances to the Bio-Oss® bovine reference.

4. Discussion

In this work, Triply Periodic Minimal Surfaces (TPMS) porous structured HA scaffolds exhibiting a Gyroid architecture with 65% porosity were prepared and investigated. The Digital Light Processing (DLP) technology via VAT photopolymerization showed appropriate to generate robust 3D-printed porous scaffolds in a reproducible way, thus comparing well with other recent reports [76,77]. The mechanical properties of the scaffolds have been here evaluated through 3-point bending tests and macrospherical indentation. The flexural strength was measured to *ca.* 7 MPa and the indicative compressive strength – calculated without taking into account the porosity of the material – reached *ca.* 4.3 MPa. These values are consistent with surgical implantation applications and previous studies outcomes [71,72].

The *in vivo* performances of the Gyroid scaffolds investigated in this work were then thoroughly evaluated, in a large animal model (skeletally mature sheep) over 6 months via in-depth analyses at a short (4 weeks) and long (26 weeks) time points. All *in vivo* outcomes were statistically compared to implantation results obtained with the exact same procedure but using again Bio-Oss® as control (internationally renowned anorganic bovine bone standard).

The local tissue response was scrutinized through both macroscopic histology observations and semi-quantitative histopathology. No abnormal observations were detected, neither about significant inflammatory reaction around the implant nor by analyzing the popliteal lymph nodes. Thus, in relation to the ISO 10993-6 stan-

dard, our data concur to demonstrate the absence of toxicity and local side effects after implantation in sheep femur.

The bone healing capacity was assessed by a bone dynamics analysis through epifluorescence using polyfluorochromes and via a quantitative histomorphometry exploration. Slightly higher signs of osteointegration were observed with the test group (Mybone® Gyroid biomaterial) compared to the control, and higher signs of bony maturation were also noted in the test biomaterial group at the two healing times. A slightly more active process of appositional mineralization occurred at the early healing time with the test group (first month), followed by a slower and normal bone turnover from week 16 in the two groups.

As pointed out in the introduction section, only few *in vivo* data are available in the literature about TPMS-structured biomaterials, and they were generally obtained from implantations in small animal models (rat, rabbit, mini-pig. and generally limited timeframes [38,53,56-60]. The positive impact of TPMS porous structures was nonetheless underlined. In particular, faster osteointegration was attained than for conventional designs. In sheep, recent outcomes [61] on biphasic calcium phosphate with Gyroid porous structure impregnated by autologous bone marrow showed promise in the repair of segmental mandibular bone defect. However, it was not clear to the authors to what extent the successful biological response was attributable to the TPMS porous structure and which part arose from the bone marrow itself. In the present study, we demonstrated that clear ossification could be achieved even without pre-impregnation with bone marrow, stressing out the intrinsic properties of the TPMS-Gyroid porous architecture with high percolation capacity as in natural trabecular bone.

In our present study on Gyroids, *in vivo* results in the sheep suggested a faster bone healing process at short term, over the Bio-Oss® reference. Conclusion of a high bone-forming ability at short term had also been drawn by testing similar Gyroids in the small animal (rat study at 4 and 8 weeks), highlighting better outcomes than an orthogonal lattice structure 3D-printed scaffold and a particulate xenograft used as controls [38].

5. Conclusions

In this work, 3D-printed hydroxyapatite scaffolds denoted MyBone® (CERHUM) with double Gyroid TPMS porous structure were fabricated by stereolithography via the VAT technology, and evaluated both from a physicochemical and biological viewpoint. The targeted pore opening was set to 900 µm for a wall thickness of 200 µm, and experimental dimensions assessed by 3D optical microscopy and SEM agreed well with the targeted sizes within the limit of light diffusion/DLP resolution. Debinding and sintering at 1270 °C (preferred to 1170 °C) allowed us to obtain cohesive scaffolds with relevant mechanical properties for guided bone regeneration in non-load bearing sites, as shown by 3-point bending tests and macrospherical indentation assays. We evidenced the percolation ability of our 3D-printed scaffolds and demonstrated their high hydrophilic character when contacted with a saline solution, even surpassing the capabilities of bovine-based Bio-Oss® reference porous blocks. XRD and FTIR analyses showed that the HA phase was not altered by the printing process, and sterilization did not affect the porous network nor the mechanical properties of the 3D construct.

The *in vivo* performances of the Gyroid scaffolds were then thoroughly evaluated in the sheep, a large animal model, for 6 months and systematically compared to the Bio-Oss® bovine standard. All data through macroscopic histology and semi-quantitative histopathology concurred to demonstrate the absence of toxicity and of local side effects after implantation in sheep femur. The scaffolds exhibited a noticeable bone healing capacity, as assessed by a bone dynamics analysis through epifluorescence with various fluorochromes, and through a quantitative histomorphometry analysis. Slightly higher signs of osteointegration and appositional mineralization were observed with the test group (Gyroid biomaterial) at short healing time compared to the Bio-Oss® control.

This study is believed to be a pilot study on the exploration of the short- and long-term *in vivo* responses of TPMS-based 3D porous (HA) scaffolds in a large animal model, and the equivalent biological response compared to Bio-Oss® – even somewhat better at short implantation time – allows definitely confirming the relevance of these engineered HA scaffolds for bone regenerative applications in view of clinical use.

This work could also serve as background study in view of the future development of self-shaping 3D-printing approaches involving various zones in the implant with gradients of densification rates or of Gyroid dimensions.

Disclosure

I.B., E.C. and G.N. mention that the compound MyBone evaluated here is commercially available from the CERHUM company, Belgium. This did not alter in any way the scientific data provided which were acquired independently.

Data availability

The data are made available by the authors upon request.

Declaration of Competing Interest

The authors declare that they have no known competing financial interests or personal relationships that could have appeared to influence the work reported in this paper.

The authors declare the following financial interests/personal relationships which may be considered as potential competing interests:

Christophe Drouet reports financial support was provided by European Union. David Grossin reports financial support was provided by European Union. Islam Bouakaz reports financial support was provided by European Union. Elisabeth Cobraiville reports financial support was provided by European Union. Gregory Nolens reports financial support was provided by European Union. David Grossin reports financial support was provided by Région Occitanie, France, under the REPERE action No. 18022525. Elisabeth Cobraiville reports financial support was provided by Federation of Wallonia and Brussels. Gregory Nolens reports financial support was provided by Federation of Wallonia and Brussels. Islam Bouakaz reports financial support was provided by Federation of Wallonia and Brussels. Islam Bouakaz, Elisabeth Cobraiville, Gregory Nolens reports a relationship with Cerhum company that includes: employment. This publication follows the ethics of research. The co-authors I.B., E.C. and G.N. mention that the compound MyBone evaluated is commercially available from the Cerhum company, Belgium. This did not alter in any way the scientific data provided which were acquired independently.

Acknowledgements

This work was supported in part by the following projects:

DOC-3D-Printing and DOC-3D-Occitanie: The DOC-3D-Printing project has received funding from the European Union's Horizon 2020 research and innovation programme under the Marie Skłodowska-Curie grant agreement No. 764935. The DOC-3D-Occitanie project has received funding from the "Région Occitanie" under the REPERE action No. 18022525.

DOVIMIS: The DOVIMIS project has received funding from the European Union's FEDER "Wallonie 2020.EU" program and the Walloon Region government under the program COOTECH MIX grant agreement No. 7931.

Supplementary materials

Supplementary material associated with this article can be found, in the online version, at doi:10.1016/j.actbio.2023.08.041.

References

[1] A.L. Boskey, Mineral-matrix interactions in bone and cartilage, Clin. Orthop. Relat. Res. (1992) 244–274.
[2] J.P. Bonjour, Calcium and phosphate: a duet of ions playing for bone health, J. Am. Coll. Nutr. 30 (5) (2011) 438S–448S.
[3] F.C.M. Driessens, J.W.E. Vandijk, R.M.H. Verbeeck, The role of bone mineral in calcium and phosphate homeostasis, Bull. Soc. Chim. Belg. 95 (5-6) (1986) 337–342.
[4] C. Huggins, The composition of bone and the function of the bone cell, Physiol. Rev. 17 (1) (1937) 119–143.
[5] C. Rey, C. Combes, C. Drouet, M.J. Glimcher, Bone mineral: update on chemical composition and structure, Osteoporos. Int. 20 (6) (2009) 1013–1021.
[6] S. Von Euw, Y. Wang, G. Laurent, C. Drouet, F. Babonneau, N. Nassif, T. Azaïs, Bone mineral: new insights into its chemical composition, Sci. Rep. 9 (1) (2019) 8456.
[7] M.L. Brandi, Microarchitecture, the key to bone quality, Rheumatology 48 (Suppl 4) (2009) (February): p. iv3-8.
[8] A. Sakkas, F. Wilde, M. Heufelder, K. Winter, A. Schramm, Autogenous bone grafts in oral implantology—is it still a "gold standard"? A consecutive review of 279 patients with 456 clinical procedures, Int. J. Implant Dentistry 3 (1) (2017) 23.
[9] S. Stevenson, Biology of bone grafts, Orthop. Clin. North Am. 30 (4) (1999) 543–552.
[10] Q. Ou, P. Wu, Z. Zhou, D. Pan, J.Y. Tang, Complication of osteo reconstruction by utilizing free vascularized fibular bone graft, BMC Surgery 20 (1) (2020) 216.
[11] E.D. Arrington, W.J. Smith, H.G. Chambers, A.L. Bucknell, N.A. Davino, Complications of iliac crest bone graft harvesting, Clin. Orthop. Relat. Res. (329) (1996) 300–309.
[12] F. Migliorini, G. La Padula, E. Torsiello, F. Spiezia, F. Oliva, N. Maffulli, Strategies for large bone defect reconstruction after trauma, infections or tumour excision: a comprehensive review of the literature, Eur. J. Med. Res. 26 (1) (2021) 118.
[13] P. Galindo-Moreno, P. Hernández-Cortés, F. Mesa, N. Carranza, G. Juodzbalys, M. Aguilar, F. O'Valle, Slow resorption of anorganic bovine bone by osteoclasts in maxillary sinus augmentation, Clin. Implant Dent. Relat. Res. 15 (6) (2013) 858–866.
[14] A. Mordenfeld, M. Hallman, C.B. Johansson, T. Albrektsson, Histological and histomorphometrical analyses of biopsies harvested 11 years after maxillary sinus floor augmentation with deproteinized bovine and autogenous bone, Clin. Oral. Implants Res. 21 (9) (2010) 961–970.
[15] T. Traini, P. Valentini, G. Iezzi, A. Piattelli, A histologic and histomorphometric evaluation of anorganic bovine bone retrieved 9 years after a sinus augmentation procedure, J. Periodontol. 78 (5) (2007) 955–961.
[16] C. Maiorana, M. Beretta, S. Salina, F. Santoro, Reduction of autogenous bone graft resorption by means of bio-oss coverage: a prospective study, Int. J. Periodontics Restorative Dent. 25 (1) (2005) 19–25.
[17] T.L. Aghaloo, P.K. Moy, Which hard tissue augmentation techniques are the most successful in furnishing bony support for implant placement? Int. J. Oral Maxillofac. Implants 22 (Suppl) (2007) 49–70.
[18] R.E. Jung, N. Fenner, C.H. Hämmerle, N.U. Zitzmann, Long-term outcome of implants placed with guided bone regeneration (GBR) using resorbable and non-resorbable membranes after 12-14 years, Clin. Oral. Implants Res. 24 (10) (2013) 1065–1073.
[19] G. Orsini, A. Scarano, M. Degidi, S. Caputi, G. Iezzi, A. Piattelli, Histological and ultrastructural evaluation of bone around Bio-Oss particles in sinus augmentation, Oral Dis. 13 (6) (2007) 586–593.
[20] H. Yoshikawa, N. Tamai, T. Murase, A. Myoui, Interconnected porous hydroxyapatite ceramics for bone tissue engineering, J. R. Soc., Interface 6 (suppl_3) (2008) S341–S348.
[21] N. Tamai, A. Myoui, T. Tomita, T. Nakase, J. Tanaka, T. Ochi, H. Yoshikawa, Novel hydroxyapatite ceramics with an interconnective porous structure exhibit superior osteoconduction in vivo, J. Biomed. Mater. Res. 59 (2002) 110–117.
[22] Z. Bal, T. Kaito, F. Korkusuz, H. Yoshikawa, Bone regeneration with hydroxyapatite-based biomaterials, Emergent Mater. 3 (4) (2020) 521–544.
[23] S. Markovic, L. Veselinovic, M.J. Lukic, L. Karanovic, I. Bracko, N. Ignjatovic, D. Uskokovic, Synthetical bone-like and biological hydroxyapatites: a comparative study of crystal structure and morphology, Biomed. Mater. 6 (4) (2011).
[24] J.M. Bouler, P. Pilet, O. Gauthier, E. Verron, Biphasic calcium phosphate ceramics for bone reconstruction: A review of biological response, Acta Biomater. 53 (2017) 1–12.
[25] K.A. Hing, Bioceramic bone graft substitutes: influence of porosity and chemistry, Int. J. Appl. Ceram. Technol. 2 (3) (2005) 184–199.
[26] O. Gauthier, J.-M. Bouler, E. Aguado, P. Pilet, G. Daculsi, Macroporous biphasic calcium phosphate ceramics: influence of macropore diameter and macroporosity percentage on bone ingrowth, Biomaterials 19 (1) (1998) 133–139.
[27] F.S.L. Bobbert, A.A. Zadpoor, Effects of bone substitute architecture and surface properties on cell response, angiogenesis, and structure of new bone, J. Mater. Chem. B 5 (31) (2017) 6175–6192.
[28] A. Bignon, J. Chouteau, J. Chevalier, G. Fantozzi, J.P. Carret, P. Chavassieux, G. Boivin, M. Melin, D. Hartmann, Effect of micro- and macroporosity of bone substitutes on their mechanical properties and cellular response, J. Mater. Sci. Mater. Med. 14 (12) (2003) 1089–1097.
[29] D. Khang, J. Lu, C. Yao, K.M. Haberstroh, T.J. Webster, The role of nanometer and sub-micron surface features on vascular and bone cell adhesion on titanium, Biomaterials 29 (8) (2008) 970–983.
[30] H.P. Yuan, K. Kurashina, J.D. de Bruijn, Y.B. Li, K. de Groot, X.D. Zhang, A preliminary study on osteoinduction of two kinds of calcium phosphate ceramics, Biomaterials 20 (19) (1999) 1799–1806.
[31] F.M. Klenke, Y. Liu, H. Yuan, E.B. Hunziker, K.A. Siebenrock, W. Hofstetter, Impact of pore size on the vascularization and osseointegration of ceramic bone substitutes in vivo, J. Biomedical Mater. Res. Part A 85A (3) (2008) 777–786.
[32] B. Feng, Z. Jinkang, W. Zhen, L. Jianxi, C. Jiang, L. Jian, M. Guolin, D. Xin, The effect of pore size on tissue ingrowth and neovascularization in porous bioceramics of controlled architecture in vivo, Biomed. Mater. 6 (1) (2011) 015007.
[33] V. Karageorgiou, D. Kaplan, Porosity of 3D biomaterial scaffolds and osteogenesis, Biomaterials 26 (27) (2005) 5474–5491.
[34] J.J. Klawitter, S.F. Hulbert, Application of porous ceramics for the attachment of load bearing internal orthopedic applications, J. Biomed. Mater. Res. 5 (6) (1971) 161–229.
[35] M.-C von Doernberg, B. von Rechenberg, M. Bohner, S. Grünenfelder, G.H. van Lenthe, R. Müller, B. Gasser, R. Mathys, G. Baroud, J. Auer, In vivo behavior of calcium phosphate scaffolds with four different pore sizes, Biomaterials 27 (30) (2006) 5186–5198.
[36] J. Li, W. Zhi, T. Xu, F. Shi, K. Duan, J. Wang, Y. Mu, J. Weng, Ectopic osteogenesis and angiogenesis regulated by porous architecture of hydroxyapatite scaffolds with similar interconnecting structure in vivo, Regener. Biomateri. 3 (5) (2016) 285–297.
[37] M. Mirkhalaf, X. Wang, A. Entezari, C.R. Dunstan, X. Jiang, H. Zreiqat, Redefining architectural effects in 3D printed scaffolds through rational design for optimal bone tissue regeneration, Appl. Mater. Today 25 (2021) 101168.
[38] D. Van hede, B. Liang, S. Anania, M. Barzegari, B. Verlée, G. Nolens, J. Pirson, L. Geris, F. Lambert, 3D-printed synthetic hydroxyapatite scaffold with in silico optimized macrostructure enhances bone formation in vivo, Adv. Funct. Mater. 32 (6) (2022) 2105002.
[39] M. Rumpler, A. Woesz, J.W.C. Dunlop, J.T. van Dongen, P. Fratzl, The effect of geometry on three-dimensional tissue growth, J. R. Soc. Interface 5 (27) (2008) 1173–1180.
[40] C.M. Bidan, K.P. Kommareddy, M. Rumpler, P. Kollmannsberger, Y.J. Bréchet, P. Fratzl, J.W. Dunlop, How linear tension converts to curvature: geometric control of bone tissue growth, PLoS One 7 (5) (2012) e36336.
[41] J. Knychala, N. Bouropoulos, C.J. Catt, O.L. Katsamenis, C.P. Please, B.G. Sengers, Pore geometry regulates early stage human bone marrow cell tissue formation and organisation, Ann. Biomed. Eng. 41 (5) (2013) 917–930.
[42] C. Drouet, R. Barré, G. Brunel, G. Dechambre, E. Benqué, C. Combes, C. Rey, Impact of calcium phosphate particle morphology on osteoconduction: an in vivo study, Bioceramics 20 (Parts 1 and 2) (2008) 361–363 p. 1371.
[43] M.L. Griffith, J.W. Halloran, Freeform fabrication of ceramics via stereolithography, J. Am. Ceram. Soc. 79 (10) (1996) 2601–2608.
[44] Z. Chen, Z. Li, J. Li, C. Liu, C. Lao, Y. Fu, C. Liu, Y. Li, P. Wang, Y. He, 3D printing of ceramics: a review, J. Eur. Ceram. Soc. 39 (4) (2019) 661–687.
[45] T.M.G. Chu, J.W. Halloran, S.J. Hollister, S.E. Feinberg, Hydroxyapatite implants with designed internal architecture, J. Mater. Sci. 12 (6) (2001) 471–478.
[46] Y. Deng, M. Mieczkowski, Three-dimensional periodic cubic membrane structure in the mitochondria of amoebae Chaos carolinensis, Protoplasma 203 (1) (1998) 16–25.
[47] V. Saranathan, C.O. Osuji, S.G. Mochrie, H. Noh, S. Narayanan, A. Sandy, E.R. Dufresne, R.O. Prum, Structure, function, and self-assembly of single network gyroid (I4132) photonic crystals in butterfly wing scales, Proc. Natl. Acad. Sci. U. S. A. 107 (26) (2010) 11676–11681.
[48] J. Iyer, T. Moore, D. Nguyen, P. Roy, J. Stolaroff, Heat transfer and pressure drop characteristics of heat exchangers based on triply periodic minimal and periodic nodal surfaces, Appl. Therm. Eng. 209 (2022) 118192.
[49] J. Seuba, S. Deville, C. Guizard, A.J. Stevenson, The effect of wall thickness distribution on mechanical reliability and strength in unidirectional porous ceramics, Sci. Technol. Adv. Mater. 17 (1) (2016) 128–135.
[50] F. Lu, R. Wu, M. Shen, L. Xie, M. Liu, Y. Li, S. Xu, L. Wan, X. Yang, C. Gao, Z. Gou, Rational design of bioceramic scaffolds with tuning pore geometry by stereolithography: microstructure evaluation and mechanical evolution, J. Eur. Ceram. Soc. 41 (2) (2021) 1672–1682.
[51] C. Goutagny, S. Hocquet, D. Hautcoeur, M. Lasgorceix, N. Somers, A. Leriche, Development of calcium phosphate suspensions suitable for the stereolithography process, Open Ceram. 7 (2021) 100167.
[52] Y. Yao, W. Qin, B. Xing, N. Sha, T. Jiao, Z. Zhao, High performance hydroxyapatite ceramics and a triply periodic minimum surface structure fabricated by digital light processing 3D printing, J. Adv. Ceram. 10 (1) (2021) 39–48.
[53] B. Charbonnier, M. Manassero, M. Bourguignon, A. Decambron, H. El-Hafci, C. Morin, D. Leon, M. Bensidoum, S. Corsia, H. Petite, D. Marchat, E. Potier,

Custom-made macroporous bioceramic implants based on triply-periodic minimal surfaces for bone defects in load-bearing sites, Acta Biomater. 109 (2020) 254–266.
[54] J.A. Ramírez, V. Ospina, A.A. Rozo, M.I. Viana, S. Ocampo, S. Restrepo, N.A. Vásquez, C. Paucar, C. García, Influence of geometry on cell proliferation of PLA and alumina scaffolds constructed by additive manufacturing, J. Mater. Res. 34 (22) (2019) 3757–3765.
[55] F.P.W. Melchels, A.M.C. Barradas, C.A. van Blitterswijk, J. de Boer, J. Feijen, D.W. Grijpma, Effects of the architecture of tissue engineering scaffolds on cell seeding and culturing, Acta Biomater. 6 (11) (2010) 4208–4217.
[56] A. Paré, B. Charbonnier, P. Tournier, C. Vignes, J. Veziers, J. Lesoeur, B. Laure, H. Bertin, G. De Pinieux, G. Cherrier, J. Guicheux, O. Gauthier, P. Corre, D. Marchat, P. Weiss, Tailored three-dimensionally printed triply periodic calcium phosphate implants: a preclinical study for craniofacial bone repair, ACS Biomater. Sci. Eng. 6 (1) (2020) 553–563.
[57] Q. Zhang, L. Ma, X. Ji, Y. He, Y. Cui, X. Liu, C. Xuan, Z. Wang, W. Yang, M. Chai, X. Shi, High-strength hydroxyapatite scaffolds with minimal surface macrostructures for load-bearing bone regeneration, Adv. Funct. Mater. 32 (33) (2022) 2204182.
[58] L. Li, J. Shi, K. Zhang, L. Yang, F. Yu, L. Zhu, H. Liang, X. Wang, Q. Jiang, Early osteointegration evaluation of porous Ti6Al4V scaffolds designed based on triply periodic minimal surface models, J. Orthop. Transl. 19 (2019) 94–105.
[59] L. Li, P. Wang, J. Jin, C. Xie, B. Xue, J. Lai, L. Zhu, Q. Jiang, The triply periodic minimal surface-based 3D printed engineering scaffold for meniscus function reconstruction, Biomater. Res. 26 (1) (2022) 45.
[60] T. Thygesen, C. Slots, M.B. Jensen, N. Ditzel, M. Kassem, L. Langhorn, M.Ø. Andersen, Comparison of off-the-shelf β-tricalcium phosphate implants with novel resorbable 3D printed implants in mandible ramus of pigs, Bone 159 (2022) 116370.
[61] A. Paré, B. Charbonnier, J. Veziers, C. Vignes, M. Dutilleul, G. De Pinieux, B. Laure, A. Bossard, A. Saucet-Zerbib, G. Touzot-Jourde, P. Weiss, P. Corre, O. Gauthier, D. Marchat, Standardized and axially vascularized calcium phosphate-based implants for segmental mandibular defects: a promising proof of concept, Acta Biomater. 154 (2022) 626–640.
[62] A.P.G. Castro, T. Pires, J.E. Santos, B.P. Gouveia, P.R. Fernandes, Permeability versus design in TPMS scaffolds, Materials 12 (2019), doi:10.3390/ma12081313.
[63] J. Santos, T. Pires, B.P. Gouveia, A.P.G. Castro, P.R. Fernandes, On the permeability of TPMS scaffolds, J. Mech. Behav. Biomed. Mater. 110 (2020) 103932.
[64] E. Yang, M. Leary, B. Lozanovski, D. Downing, M. Mazur, A. Sarker, A. Khorasani, A. Jones, T. Maconachie, S. Bateman, M. Easton, M. Qian, P. Choong, M. Brandt, Effect of geometry on the mechanical properties of Ti-6Al-4V Gyroid structures fabricated via SLM: a numerical study, Mater. Des. 184 (2019) 108165.
[65] V. Glatt, C.H. Evans, K. Tetsworth, A concert between biology and biomechanics: the influence of the mechanical environment on bone healing, Front. Physiol. 7 (2016) 678.
[66] P.J. Hine, T. Leejarkpai, E. Khosravi, R.A. Duckett, W.J. Feast, Structure property relationships in linear and cross-linked poly(imidonorbornenes) prepared using ring opening metathesis polymerisation (ROMP), Polymer 42 (23) (2001) 9413–9422.
[67] E. Andrzejewska, Photopolymerization kinetics of multifunctional monomers, Prog. Polym. Sci. 26 (4) (2001) 605–665.
[68] N. Jackson, M. Assad, D. Vollmer, J. Stanley, M. Chagnon, Histopathological evaluation of orthopedic medical devices: the state-of-the-art in animal models, imaging, and histomorphometry techniques, Toxicol. Pathol. 47 (3) (2019) 280–296.
[69] Y. Pei, F. Agostini, F. Skoczylas, Rehydration on heat-treated cementitious materials up to 700°C-coupled transport properties characterization, Constr. Build. Mater. 144 (2017) 650–662.
[70] F. Pennella, G. Cerino, D. Massai, D. Gallo, G. Falvo D'Urso Labate, A. Schiavi, M.A. Deriu, A. Audenino, U. Morbiducci, A survey of methods for the evaluation of tissue engineering scaffold permeability, Ann. Biomed. Eng. 41 (10) (2013) 2027–2041.
[71] A. Paknahad, N.W. Kucko, S.C.G. Leeuwenburgh, L.J. Sluys, Experimental and numerical analysis on bending and tensile failure behavior of calcium phosphate cements, J. Mech. Behav. Biomed. Mater. 103 (2020) 103565.
[72] H.Y. Yasuda, S. Mahara, T. Nishiyama, Y. Umakoshi, Preparation of hydroxyapatite/α-tricalcium phosphate composites by colloidal process, Sci. Technol. Adv. Mater. 3 (1) (2002) 29–33.
[73] S. Sagadevan, P. Murugasen, Novel analysis on the influence of tip radius and shape of the nanoindenter on the hardness of materials, Procedia Mater. Sci. 6 (2014) 1871–1878.
[74] L. Zhang, S. Feih, S. Daynes, S. Chang, M.Y. Wang, J. Wei, W.F. Lu, Pseudo-ductile fracture of 3D printed alumina triply periodic minimal surface structures, J. Eur. Ceram. Soc. 40 (2) (2020) 408–416.
[75] L. Le Guéhennec, D. Van hede, E. Plougonven, G. Nolens, B. Verlée, M.-C. De Pauw, F. Lambert, In vitro and in vivo biocompatibility of calcium-phosphate scaffolds three-dimensional printed by stereolithography for bone regeneration, J. Biomedical Mater. Res. Part A 108 (3) (2020) 412–425.
[76] N. Isaacson, K. Lopez-Ambrosio, L. Chubb, N. Waanders, E. Hoffmann, C. Witt, S. James, D.A. Prawel, Compressive properties and failure behavior of photocast hydroxyapatite gyroid scaffolds vary with porosity, J. Biomater. Appl. 37 (1) (2022) 55–76.
[77] J.-W. Lee, Y.H. Lee, H. Lee, Y.H. Koh, H.E. Kim, Improving mechanical properties of porous calcium phosphate scaffolds by constructing elongated gyroid structures using digital light processing, Ceram. Int. 47 (3) (2021) 3252–3258.